Angewandte Chemie
GDCh
Eine Zeitschrift der Gesellschaft Deutscher Chemiker
www.angewandte.de

Akzeptierter Artikel

Titel: Suppressing Interfacial Charge Recombination in Electron Transport Layer-Free Perovskite Solar Cells with Efficiency Exceeding 21%

Autoren: Wu-Qiang Wu, Jin-Feng Liao, Jun-Xing Zhong, Yang-Fan Xu, Lianzhou Wang, and Jinsong Huang

Zitierweise: *Angew. Chem. Int. Ed.* 10.1002/anie.202005680

Link zur VoR: https://doi.org/10.1002/anie.202005680

WILEY-VCH

RESEARCH ARTICLE WILEY-VCH

Suppressing Interfacial Charge Recombination in Electron Transport Layer-Free Perovskite Solar Cells with Efficiency Exceeding 21%

Wu-Qiang Wu[#],*[a][b] Jin-Feng Liao[#],[a] Jun-Xing Zhong,[a] Yang-Fan Xu,[a] Lianzhou Wang,*[b] and Jinsong Huang*[c]

[a] Dr. W. Q. Wu, Dr. J. F. Liao, J. X. Zhong, Dr. Y. F. Xu
MOE Key Laboratory of Bioinorganic and Synthetic Chemistry, Lehn Institute of Functional Materials, School of Chemistry, Sun Yat-sen University, Guangzhou 510275, P. R. China.
E-mail: wuwq36@mail.sysu.edu.cn
[b] Dr. W. Q Wu, Prof. L. Wang
Nanomaterials Centre, School of Chemical Engineering and Australian Institute for Bioengineering and Nanotechnology, The University of Queensland, Brisbane, QLD 4072, Australia.
E-mail: l.wang@uq.edu.au
[c] Prof. J. Huang
Department of Applied Physical Sciences, University of North Carolina, Chapel Hill, North Carolina 27599, United States
E-mail: jhuang@unc.edu
# These authors contributed equally to this work.

Supporting information for this article is given via a link at the end of the document.

Abstract: The performances of reported electron transport layer (ETL)-free perovskite solar cells (PSCs) are still inferior to ETL-containing devices. This is mainly due to severe interfacial charge recombination occurred at the transparent conducting oxide (TCO)/perovskite interface, where the photo-injected electrons in the TCO can travel back to recombine with holes in the perovskite layer. Herein, we for the first time demonstrate that a non-annealed, insulating, amorphous metal oxyhydroxide, atomic-scale thin interlayer (~3 nm) between the TCO and perovskite facilitates electron tunnelling and suppresses the interfacial charge recombination. This largely reduced the interfacial charge recombination loss and achieved a record efficiency of 21.1% for *n-i-p* structured ETL-free PSCs, outperforming their ETL-containing metal oxide counterparts (18.7%), as well as narrowing the efficiency gap with high-efficiency PSCs employing highly crystalline TiO_2 ETLs.

Introduction

The past decade has witnessed striking achievements in perovskite solar cells (PSCs) owing to the intriguing optoelectronic properties of organic-inorganic lead halide perovskite materials, such as prominent light absorption coefficients, tunable bandgaps and ease of solution processability.[1-3] To date, almost all reported high-efficiency PSCs are based on a layer-by-layer stacking architecture with a perovskite layer sandwiched between two carrier transport layers (CTLs), namely, the electron transport layer (ETL) and the hole transport layer (HTL), and completed with a metal electrode on top. Unfortunately, coating of the multiple layers is time-consuming, while the cost of the CTL materials is normally high, despite perovskite materials being cheap.[4,5] In addition, the commonly used metal oxide ETLs, such as TiO_2 and SnO_2, require an energy-consuming annealing process (>150 °C) to ensure good charge transport characteristic. All of aforementioned aspects would inevitably increase the complexity and cost of device production.[6-11] Other fascinating optoelectronic properties of these magic perovskite materials, e.g. ambipolar charge transport capability, low exciton dissociation energy and long charge diffusion length, point to the great potential for constructing high-performance, ETL-free PSCs, which is thought to be a perfect solution to address the dilemma of balancing high efficiency and low production cost.[12] Owing to continuous research efforts to optimize the materials, interfaces, device structures and fabrication processes, the power conversion efficiencies (PCEs) of state-of-the-art ETL-free PSCs already exceed 20%, which is approaching the certified PCE as high as 25.2% for their ETL-containing counterpart.[13-19] The next step is to further reduce the efficiency gap between the ETL-free 'simplified' PSCs and devices with standard architecture, but this is still a great challenge.

Some reports have shown that electron injection from the intrinsic perovskite layer to the transparent conducting oxide (TCO) is energy favorable, hence electron extraction at the TCO/perovskite interface is only a moderate concern even in the absence of the ETL.[20-23] In contrast, one should mostly worry about under-optimized contacts that result in unbalanced charge transfer and unwanted interfacial charge recombination in ETL-free devices, which dominate the interfacial recombination losses, thus lowering the photovoltage (V_{oc}) and PCE. Surface modification of the TCO substrate with a thin layer of organic material has been demonstrated to mitigate the mismatched energy level alignment between the TCO and perovskite. This was achieved by tuning the surface work functions of the TCO, forming an interfacial dipole and/or favorably influencing the band bending direction at the TCO/perovskite interface for facilitated charge extraction and suppressed charge recombination.[24,25] On one hand, such organic modifiers are criticized for their high cost and hygroscopic characteristic.[15,16,26] Yet, on the other hand, these interfacial modification layers are made by a spin-coating process, which is not compatible with scalable fabrication. Moreover, it remains a big challenge to form a dense and robust interlayer with a thickness of only several nanometers, unless it can be prepared via an in-situ growth process. Worse still, in some cases, the annealed or crystallized

interlayer is semiconducting, which enables charge recombination at the TCO/perovskite interface, thus incurring interfacial charge recombination. Hence, it is highly desirable to fabricate a thin but dense, amorphous, inorganic interlayer in a low-cost and scalable manner, that can play multifunctional roles and optimize the contact properties at the TCO/perovskite interface for more efficient ETL-free PSCs.

Herein, modifying the TCO substrate with an atomic-scale thin amorphous niobium oxyhydroxide (a-NbOH) layer has enabled high-performance, ETL-free PSCs with >21% efficiency, negligible hysteresis and enhanced operational stability. This, to the best of our knowledge, is the record efficiency for PSCs with such a simplified device structure. The embedded a-NbOH interlayer, between the TCO and perovskite, not only served as an insulating barrier for reduced interfacial charge recombination loss, but also functioned as an electron tunneling contact for facilitated electron extraction and reinforced hole blocking. The surface of the a-NbOH layer is rich in hydroxyl groups, which promote the crystal growth necessary to obtain high-quality perovskite films with improved crystallinity, large grain sizes and low trap densities. Notably, this thin, dense, non-crystalline, inorganic interlayer modification strategy provides additional promise to fabricate large area, ETL-free PSCs, demonstrating a decent efficiency approaching 20.0% for an ETL-free device with an aperture of 1.1 cm^2.

Results and Discussion

As illustrated in Figure 1a, an a-MOH layer was prepared via a facile, one-step, hydrothermal-assisted hydrolysis of an aqueous metal chloride solution at low temperature ranging from 40 °C to 130 °C, resulting in the self-assembly of a nanostructured thin film on a 2 cm*2 cm fluorine-doped tin oxide (FTO) glass substrate (see details in Experimental Section). Different metal chlorides (MCl_x), namely, $TiCl_4$, $NbCl_5$, $SnCl_4$, WCl_6, $ZnCl_2$, $MgCl_2$ and $ZrOCl_2$, were employed to validate the versatility of this solution-processed method to achieve in-situ coatings of different a-MOH thin layers on FTO glass. Typically, the surface of FTO turned coarse after treatment with $TiCl_4$, $NbCl_5$, $SnCl_4$ and $ZrOCl_2$ (Figure 1e, 1f and S1). By contrast, no apparent change was observed when using WCl_6, $ZnCl_2$ and $MgCl_2$ (Figure S1), probably due to the different hydrolysis rates of the MCl_x and lattice matching degree between FTO and the different a-MOHs.[27-29] We conducted a preliminary materials screening by simply evaluating the photovoltaic performances of ETL-free devices based on different a-MOH interlayers. Encouragingly, the a-MOH modifications achieved using different MCl_x played a mostly positive role in boosting the device performances. The only exception was $ZnCl_2$, which lowered the efficiency (Figure S2 and Table S1). In addition, it is found that after the surface modification of FTO with $SnCl_4$, $TiCl_4$, $ZrOCl_2$ and $NbCl_5$, the hysteresis index (HI) of the device was significantly reduced from 9.7% to 4.7%, 0.8%, 0.6% and 0.2%, respectively (Figure S3 and Table S2). Specifically, $NbCl_5$ treatment was considered to be optimal, and thus selected as being representative in the following studies for a fundamental study on the effectiveness of MCl_x treatment on boosting the PCE of the ETL-free PSCs.

X-ray photoelectron spectroscopy (XPS) was used to determine the chemical state of the elements and the content of the surface functional groups in the $NbCl_5$-processed sample. The peaks located at binding energies of 207 eV and 210 eV were indexed to the signal of Nb^{5+}, affirming the successful modification of Nb-containing species on the FTO surface (Figure 1b and S4). Further analysis of the high-resolution O 1s signal in XPS spectra implies that the contents of hydroxyl groups on the surface of Nb_2O_5 film (23%) is significantly lower than that of a-NbOH counterpart (73%) (Figure 1c and S5). We inferred that the low-temperature treatment of FTO glass with $NbCl_5$ aqueous solution led to the formation of amorphous species. In addition, the XPS spectra in Figure 1d showing a plot of the Pb 4f signal was shifted to a lower binding energy upon a-NbOH surface modification, indicative of increased electron density surrounding Pb^{2+} species, owing to their strong coordination with lone pair electrons in -OH groups. This chemical interaction favorably assists the crystal growth and film formation of perovskite, as well as promoting its connection and adhesion to the underlying FTO substrate despite the absence of an ETL.[3,29,30]

The morphology, film thickness and surface coverage of the a-NbOH thin film on FTO glass play a crucial role in tuning the balance between the charge extraction and hole blocking properties of the PSC devices.[31] As shown in Figures S6-S8, we systematically optimized the surface topographies and structural properties (i.e. thickness and coverage) of the a-NbOH films by varying the $NbCl_5$ precursor concentration, hydrothermal reaction temperature and hydrolysis time. For the growth of the a-NbOH layer, too fast a nucleation rate or overgrowth driven by an increased reaction temperature and prolonged reaction time produced undesirably thick films and/or too large particle sizes, both of which are adverse to charge transfer and collection. Conversely, inadequate growth time and temperature resulted in poor uniformity and inferior coverage by the a-NbOH layer on the FTO surface. In this case, direct contact between the perovskite and FTO induces severe interfacial charge recombination. Preliminary studies of the photovoltaic performances and corresponding photovoltaic parameters of PSCs based on these a-NbOH films are presented in Tables S3-S5. The optimal performance was achieved for the PSC based on the a-NbOH interlayer prepared through the hydrolysis of 22 mM $NbCl_5$ at 130 °C for 3 h, which resulted in the most uniform coating of a-NbOH with a thickness of approximately 3 nm on the profile of the FTO pyramidal surface, as is visualized in Figure 1f-g and S9. In addition to the PCE, the thickness of the a-NbOH layer was also found to play a critical role in affecting the *J-V* hysteresis, and the PSCs fabricated with ~3 nm a-NbOH layer showcased the smallest HI value of 0.2% (Figure S10 and Table S3).

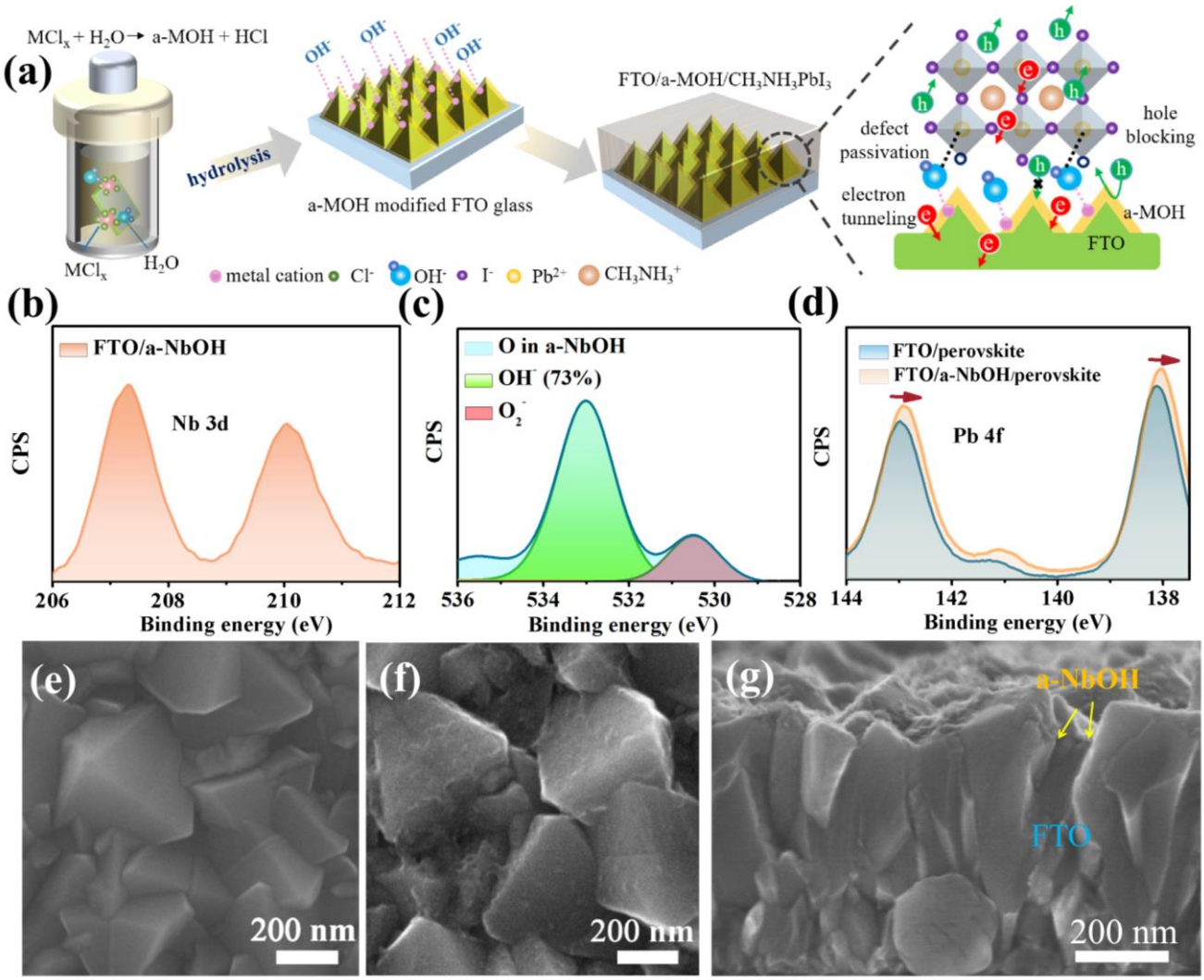

Figure 1. (a) Sketch showing the hydrothermal process to coat the FTO surface with an ultrathin a-MOH layer, and the multifuctions of a-MOH interlayer on facilitated electron tunneling, hole blocking and defect passivation. (b)The high-resolution XPS spectra of Nb 3d signal. (c) Fitted XPS result of O 1s in a-NbOH with the relative surface content of –OH in brackets (derived from the integrated areas of the fitted peaks). (d) XPS spectra for the Pb 4f signal of $MAPbI_3$ film deposited on pristine FTO and FTO/a-NbOH substrates. Scanning electron microscopy (SEM) images of (e) pristine FTO and (f) FTO/a-NbOH. (g) Cross-sectional SEM image of FTO/a-NbOH.

The hydrothermally processed a-NbOH film can be directly used as a modification interlayer without further annealing, which is beneficial to retaining its amorphous and insulating features. For comparison, a Nb_2O_5 counterpart was prepared via high temperature annealing of as-prepared a-NbOH at 600 °C for 1 h. The X-ray diffraction (XRD) pattern of the FTO/a-NbOH sample was indexed to the rutile tetragonal SnO_2 component of the FTO glass (Figure S11a). Similarly, there are no characteristic XRD signals of Nb_2O_5 in the glass/a-NbOH sample (Figure S11b), suggesting the amorphous character of the as-grown a-NbOH thin film. To exclude the effect of the substrate, we directly collected the powders from solution immediately after the hydrothermal reaction. The freshly collected powder showed a typical amorphous XRD pattern, whereas the high-temperature annealed powder exhibited distinct XRD signals, which were indexed as highly crystalline Nb_2O_5 (Figure 2a). We scratched the a-NbOH sample from the FTO glass substrate for a transmission electron microscope (TEM) study. The a-NbOH sample showed a blurry bulk morphology and amorphous features, as confirmed by the selected area electron diffraction (SAED) pattern (Figure 2b). After annealing, angular nanocrystals were clearly observed, accompanied by the appearance of a distinct lattice fringe in high-resolution TEM images, together with a typical crystalline ring-like diffraction fringe in the SAED pattern (Figure 2c), suggesting increased crystallinity upon high temperature calcination. Therefore, we concluded that the formation of non-crystalline a-NbOH can be ascribed to the low temperature hydrothermal process without subsequent annealing.

The a-NbOH surface modification enhances the wettability of the perovskite precursor on the FTO substrate, owing to the presence of a high surface -OH content, as evidenced by the smaller contact angle (Figure S12). The superior wettability and favorable chemical interaction between perovskite species and the surface hydroxyl-rich substrate ultimately benefits the growth of perovskite films with improved quality, e.g. enhanced crystallinity, dense packing and uniform surface coverage.[30,32] As seen in Figure 2d, all characteristic XRD peaks of $MAPbI_3$ deposited on FTO/a-NbOH substrate have been intensified, confirming the increased crystallinity of the perovskite film.

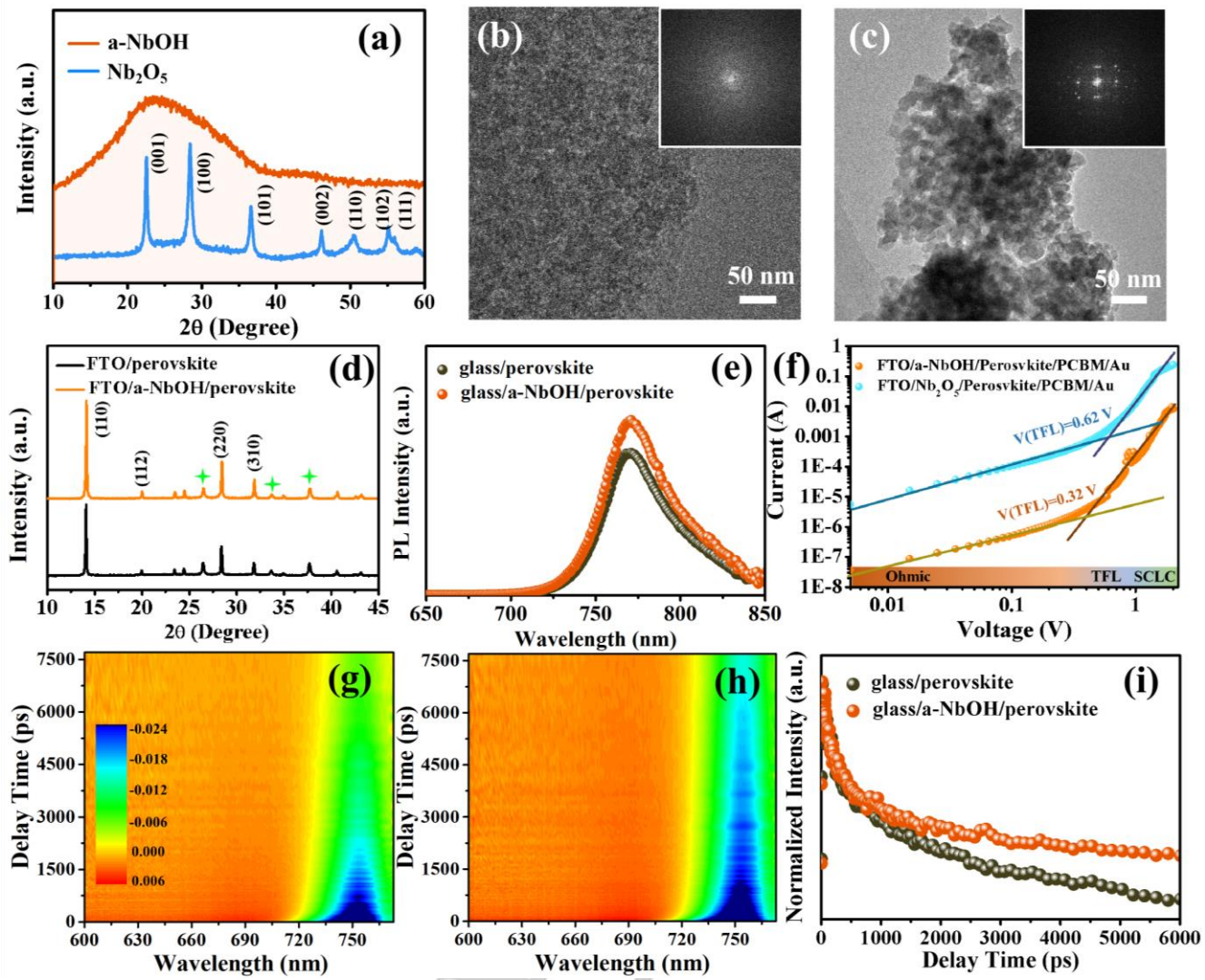

Figure 2. (a) XRD patterns of a-NbOH and Nb_2O_5 powders. TEM images and inset SAED images of (b) a-NbOH powder and (c) Nb_2O_5 powder. (d) XRD patterns (peaks marked with green asterisks are signals assigned to the FTO substrate) and (e) steady-state PL intensities of perovskite films deposited on glass and glass/a-NbOH substrates. (f) Dark *I-V* characteristics of the electron-only devices based on a-NbOH or Nb_2O_5 interlayers. Contour plot fs-TA spectra of perovskite films deposited on (g) glass and (h) glass/a-NbOH, and (i) the corresponding dynamic TA decay probed at the GSB peak.

In addition, the a-NbOH modification induced the growth of perovskite films with large grains that grew perpendicular to the underlying substrate, which then ensured good contact at the TCO/perovskite interface for better charge collection (Figure S13). For comparison, deep ravines were present in the perovskite films fabricated on the high-temperature annealed FTO/Nb_2O_5 substrates. These ravines will provide a route for direct contact between the HTL and FTO, thus causing short-circuit or device shunting. The enhanced crystallinity and enlarged grain sizes are beneficial to reducing the densities of defects and/or trap states, thus suppressing non-radiative recombination in the bulk perovskite film, as confirmed by the enhanced photoluminescence (PL) intensity for the perovskite film deposited on the glass/a-NbOH substrate (Figure 2e). Similar conclusions were drawn from the femtosecond (fs) transient absorption (TA) tests shown in Figure 2g and h. The signal intensity of the ground-state bleaching (GSB) peak at ~750 nm reflects the photo-induced carrier population in the $MAPbI_3$ perovskite layer. The photo-induced absorption change (ΔA, representing GSB signal intensity change) gradually decreased with prolonged delay time, indicating heightened recombination between photo-induced electrons and holes in the $MAPbI_3$ (Figure S14). The GSB peak intensity for the same delay time was much stronger for the perovskite film deposited on the a-NbOH interlayer, agreeing well with the retarded carrier recombination dynamic in the improved quality of neat perovskite film with reduced trap densities (Figure 2i, Table S6)

The electronic trap-state densities in the perovskite layer can be estimated by a space-charge limited current (SCLC) measurement for the electron-only device with a structure of FTO/interlayer/perovskite/PCBM/Au, where the interlayer is a-NbOH or Nb_2O_5, and PCBM is [6,6]-phenyl-C_{61}-butyric acid methyl ester.[33] Figure 2f depicts the dark current-voltage (*I-V*) curves of the corresponding devices. In general, the linear region at low bias represents the ohmic response, followed by a trap-filling process at high bias.[33,34] The trap-filled limit voltage (V_{TFL}) was estimated to be 0.39 V for the a-NbOH based device, 30% lower than the Nb_2O_5-based counterpart (0.62 V). The trap-state densities can be calculated as

$$N_{trap} = \frac{2\varepsilon_0\varepsilon_r V_{TFL}}{ed^2}$$

where ε_0 is the vacuum permittivity, ε_r is the relative dielectric constant of perovskite, e is the charge constant, and d is the thickness of the perovskite film. The trap-state densities in the a-NbOH based device were 8.6×10^{15} cm^{-3}, which was nearly half that of Nb_2O_5 (1.38×10^{16} cm^{-3}), suggesting a reduction in trap-state densities was induced by the high-quality perovskite films with enhanced crystallinities and enlarged grain sizes.[33,35]

We then investigated the optoelectronic properties and charge carrier dynamics of the devices and/or relevant interfaces based on perovskite films deposited on non-crystalline a-NbOH and crystalline Nb_2O_5. The carrier transfer and recombination dynamics at the a-NbOH/perovskite or Nb_2O_5/perovskite interfaces were studied by analyzing the steady-state PL spectra. Stronger PL quenching was observed in the Nb_2O_5/$MAPbI_3$ film, suggesting that the photo-generated electrons in the perovskite were efficiently extracted out by the adjacent highly crystalline, semiconducting Nb_2O_5, which may have contributed to the increased J_{sc} of the Nb_2O_5-based PSC, owing to the facilitated charge extraction rate.[36] Surprisingly, a considerable degree of PL quenching was also observed for the FTO/a-NbOH/perovskite sample, as compared to the reference FTO/perovskite sample, where the interfacial carrier dynamics was dominated by electron-hole recombination (Figure S15). Hence, there was still charge transfer behavior occurring at the a-NbOH/perovskite interface, despite the a-NbOH itself being amorphous and insulating. We inferred that the charge transfer was achieved by efficient interfacial charge tunneling, that profited from the ultrathin characteristic of the a-NbOH interlayer. Additionally, charge collection from the perovskite to the FTO electrode is sufficiently ensured. To determine whether the tunneling charges were electrons or holes, we performed conductive AFM (c-AFM) measurements to quantify the photocurrent and local dark current of the devices assembled with or without an a-NbOH modification layer at the nanoscopic level (Figure 3a-3d). For the photocurrent measurement, the devices featured a structure of FTO/poly(bis(4-phenyl)(2,4,6-trimethylphenyl)amine) (PTAA)/perovskite/C_{60} with or without a-NbOH on top, and were illuminated by a white light source (Figure 3a and 3b). In the presence of the a-NbOH interlayer, the local photocurrent through the perovskite grains was significantly increased from -1.45 pA to -2.0 pA (Figure 3e and 3f), indicating the beneficial function of the a-NbOH interlayer modification in facilitating electron collection, thus enhancing the photocurrent output.

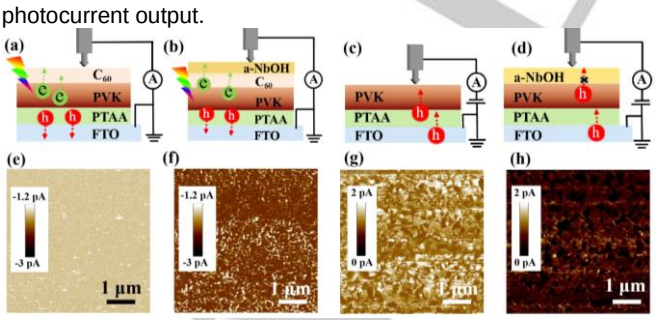

Figure 3. The c-AFM setup and corresponding photocurrent mapping on devices with structures (a, e) FTO/PTAA/perovskite/C_{60} and (b, f) FTO/PTAA/perovskite/C_{60}/a-NbOH. The c-AFM setup and corresponding local dark current mapping under bias on devices with structures of (c, g) FTO/PTAA/perovskite and (d, h) FTO/PTAA/perovskite/a-NbOH.

For the local dark current measurements, the devices featured a structure of FTO/PTAA/perovskite with or without a-NbOH on top, and were excited by an applied bias (Figure 3c and 3d). In the case of the a-NbOH modification on the perovskite, the average current was about 0.4 pA, three folds lower than that of the device without a-NbOH, ~1.2 pA (Figure 3g and h). The increased photocurrent (i.e. electron current) together with the decreased local dark current (i.e. hole current) synergistically authenticated the positive dual roles of a-NbOH in optimizing the electronic properties of perovskite-based devices, namely, serving as a tunneling layer for electron extraction and a spatial barrier for hole blocking, which are quite promising and suitable to be employed in ETL-free PSCs.[37]

To further distinguish the a-MOH interlayer from the conventionally used, highly crystalline, metal oxide ETLs, we carried out characterizations to compare their different interfacial charge transfer and recombination dynamics. The conventional ETL/perovskite interface often exhibits an ultrafast photo-excited carrier charge transfer dynamic with a timescale of picoseconds, which raised a question about the timescale of electron tunneling occurring in FTO/a-NbOH or Nb_2O_5/perovskite samples. This was answered quantitatively by fs-TA measurements. As shown in Figure 4a and 4b, contour plots of the TA spectra revealed that the ΔA of the GSB signal gradually decreased with prolonged delay time, indicating that the photo-induced electrons in perovskite were progressively extracted out to the FTO substrates. Moreover, the GSB peak intensity of the perovskite on the FTO/a-NbOH substrate did not fade as promptly as in the FTO/Nb_2O_5 sample. This phenomenon was further confirmed by the decay kinetics of the GSB, which were fitted with a three exponential decay equation (Figure S16 and Table S7). The two ultrafast decay time components (τ_1 and τ_2), on a timescale of picoseconds, can be interpreted as the process of photogenerated electrons being extracted out from the perovskite layer, while the slow decay time component (τ_3), on a nanosecond level, can be ascribed to the processes of excited-state decay or trap-assisted recombination in the bulk perovskite and/or at the relevant interfaces, as reported previously.[36] A considerably faster electron extraction time was found for the Nb_2O_5-based sample (99–555 ps) compared to the a-NbOH based sample (112-797 ps). According to the previous report,[38] the contribution of hole lifetime to the GSB signal is about 30%. Considering most of the photo-induced electrons were preferentially collected by the neighboring contact/electrode owing to the matched energy level alignment, it is reasonably to attribute the τ_3, which takes up a similar contribution proportion (i.e. 23%-27%) of the overall lifetime, to the hole lifetime in perovskite layer. In this case, the residual photo-induced holes in perovskite are supposed to be mainly consumed by interfacial charge recombination, namely, the electrons travel back to recombine with holes in perovskite. Notably, the τ_3 of the a-NbOH based sample was 1-fold longer than the Nb_2O_5 counterpart (5570 ps versus 2500 ps), suggesting the prolonged hole lifetime in the former case. This result suggested the inhibition of electron injection from FTO to the perovskite owing to the a-NbOH interlayer serving as an insulating spatial barrier to suppress the interfacial charge recombination, thus suppressing the interfacial charge recombination and reducing current leakage. In contrast, there remains a higher chance that photo-injected electrons accumulated in crystalline Nb_2O_5 ETL or FTO could promptly travel back to recombine with holes in the perovskite, thereby leading to severe charge recombination and thus energy loss, as depicted in Figure 4c and d. As shown in Figure S17, the carrier

lifetime is longer in an a-NbOH based PSC, even in the absence of an ETL, confirming the suppressed charge recombination and agreeing with the high V_{oc} for the PSC based on the a-NbOH interlayer.

The multifaceted functions of an ultrathin, amorphous metal oxide when employed as an interfacial modification layer in PSCs, and the necessity of modifying the TCO substrate for tackling the issue of interfacial charge recombination in ETL-free devices can be summarized as follows. First, although the non-annealed a-NbOH interlayer cannot function as an ETL by itself to extract electrons due to its low crystallinity and insulating properties, it still enables electron tunneling from perovskite to FTO via an ultrathin channel (~3 nm). Second, it advantageously serves as a spatial barrier to avoid direct contact of the perovskite with the FTO, and can efficiently block hole injection. Third, the a-NbOH can serve as an interfacial linker and passivator to reinforce the contact at the FTO/perovskite interface, modulate the crystal growth and film formation of perovskite, as well as relieve defect-induced non-radiative charge recombination within bulk perovskite film and/or an adjacent interface. Last but not least, the insulating properties of ultra-thin a-NbOH interlayer, which in turns, is more robust in suppressing the interfacial charge recombination at the FTO/perovskite interface than the commonly used highly crystalline ETL, thus enhancing the carrier lifetime and reducing the interfacial charge recombination loss. (Figure 1a and Figure 4c and 4d).

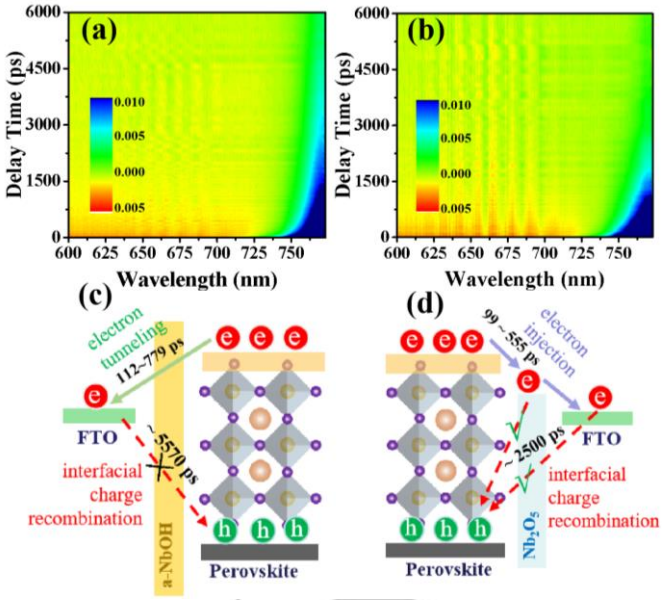

Figure 4. Contour plots of the fs-TA spectra of perovskite films deposited on (a) FTO/a-NbOH and (b) FTO/Nb_2O_5 substrates. (Schematic illustration of electron extraction and recombination at (c) FTO/a-NbOH/perovskite and (d) FTO/Nb_2O_5/perovskite interfaces.

Given the multiple advantages of the ultrathin a-NbOH interlayer, we have demonstrated efficient and stable ETL-free PSCs as a proof-of-concept. We fabricated the ETL-free PSC with a conventional *n-i-p* architecture of FTO/a-NbOH/perovskite/HTL/Au, as illustrated in Figure 5a. Figure 5b shows typical *J-V* curves for PSCs based on $MAPbI_3$ perovskite films deposited on pristine FTO, FTO/a-NbOH and FTO/Nb_2O_5 substrates, and the corresponding photovoltaic parameters are summarized in Table S8. The ETL-free device with the non-annealed a-NbOH interlayer delivered a maximum PCE of 20.0% along with a J_{sc} of 22.2 mA cm^{-2}, a V_{oc} up to 1.14 V and a *FF* of 0.79, which was higher than that of the PSCs constructed with either pure FTO glass (a PCE of 12.8%, along with a J_{sc} of 19.0 mA cm^{-2}, a V_{oc} of 1.02 V and a *FF* of 0.66) or the high-temperature sintered Nb_2O_5 (a PCE of 18.7%, along with a J_{sc} of 22.5 mA cm^{-2}, a V_{oc} of 1.08 V and a *FF* of 0.77). This demonstrates the effectiveness of utilizing an ultrathin a-MOH interlayer to construct efficient PSCs in the absence of ETLs, while weakening the necessity to employ highly crystalline metal oxide ETLs to fabricate high-efficiency devices. The external quantum efficiency (EQE) spectra of the PSCs based on bare FTO, Nb_2O_5 and a-NbOH were displayed in Figure S18. The integrated J_{sc} (i.e. 18.4, 22.0 and 21.6 mA cm^{-2} for FTO, Nb_2O_5 and a-NbOH based PSCs, respectively) matched well with the J_{sc} obtained from the *J-V* curves (Figure 5b), with <3% discrepancy. Although the J_{sc} was slightly lower than that of the device with the crystalline Nb_2O_5, the V_{oc} and *FF* were increased significantly for the a-NbOH based PSC, which was attributed to suppression of the interfacial charge recombination (i.e. prolonged carrier lifetime, as shown in Figure S17) induced by the a-NbOH interlayer. The *J-V* hysteresis of the PSCs based on bare FTO, Nb_2O_5 and a-NbOH were also investigated, as is shown in Figure S19 and Table S9. The PSC based on the a-NbOH showcased the smallest HI value of 0.2%, as compared to that of the devices based on bare FTO (9.7%) and Nb_2O_5 (2.7%). We further demonstrate the versatility of this a-MOH interlayer modification strategy by constructing ETL-free PSCs based on other perovskite compositions, e.g. the mixed cation $Cs_{0.07}FA_{0.70}MA_{0.23}PbI_3$ (see Experimental Section). An SEM image of the $Cs_{0.07}FA_{0.70}MA_{0.23}PbI_3$ perovskite film showed good uniformity and surface coverage when deposited on the a-NbOH layer (Figure S20). Encouragingly, the PCE was further enhanced up to 21.1% at reverse scan, with a J_{sc} of 23 mA cm^{-2}, a V_{oc} of 1.16 V and a *FF* of 0.79, while a PCE of 20.8% was achieved at forward scan (J_{sc}=23 mA cm^{-2}, V_{oc}=1.16 V, *FF*=0.78) (Figure 5c). To consolidate the reliability of the device performance, the steady-state power output was measured under an applied bias at the maximum power point of 0.96 V, yielding a stabilized PCE of 20.6% under AM 1.5G one sun illumination. This result was consistent with the PCE measured from the *J-V* curves (Figure 5d).[7,39] The EQE spectrum exhibited a broad plateau above 80% over the wavelength region ranging from 400 nm to 780 nm, while the integrated photocurrent density (22.5 mA cm^{-2}) matched well with the J_{sc} obtained from the *J-V* curves with <3% discrepancy (Figure S21). The PCE histogram collected from a batch of 30 devices is presented in Figure 5e, which illustrates that more than 83% of the cells achieved PCEs above 20%, while more than 10% of the devices obtained PCEs over 21% under one sun illumination. This result validates the high performance and high reproducibility of these ETL-free PSCs based on an a-NbOH interlayer. The operational stability of the devices with a structure of FTO/a-NbOH/perovskite/PTAA/Au were also tested under continuous one sun illumination. Encouragingly, the a-NbOH modified ETL-free PSC exhibited enhanced stability, with over 96% of its original PCE retained after 500 h (Figure 5f), compared with only 60% of initial PCE retained for the Nb_2O_5-based cells. These results corroborate the superiority of the non-annealed a-NbOH interlayer over the high temperature-annealed Nb_2O_5 for improving both device efficiency and stability, even though the a-NbOH forms part of an ETL-free device. The enhanced

operational stability can be attributed to the improved quality of the perovskite films for reduced trap-state densities, as well as the beneficial charge tunneling and interfacial passivation effect at the modified FTO/perovskite interface for suppressed charge recombination and enhanced charge collection.[40,41] To demonstrate the practicality of this work towards the mass production of PSCs, larger-area devices with a 1.1 cm^2 aperture were fabricated.[12,22] The *J-V* characteristics of the optimal device are shown in Figure S22. The champion 1.1 cm^2 cell achieved a PCE approaching 20.0%, which attests to the uniformity of the a-NbOH film on a square-centimeter scale, and further suggests the efficacy of utilizing a non-annealed, solution-processed, ultrathin a-MOH interlayer towards the potentially cost-effective commercialization of PSCs. The slight drop of photovoltaic parameters for the large-area devices compared to their small-area counterparts were primarily due to the increased series resistance of the larger devices.

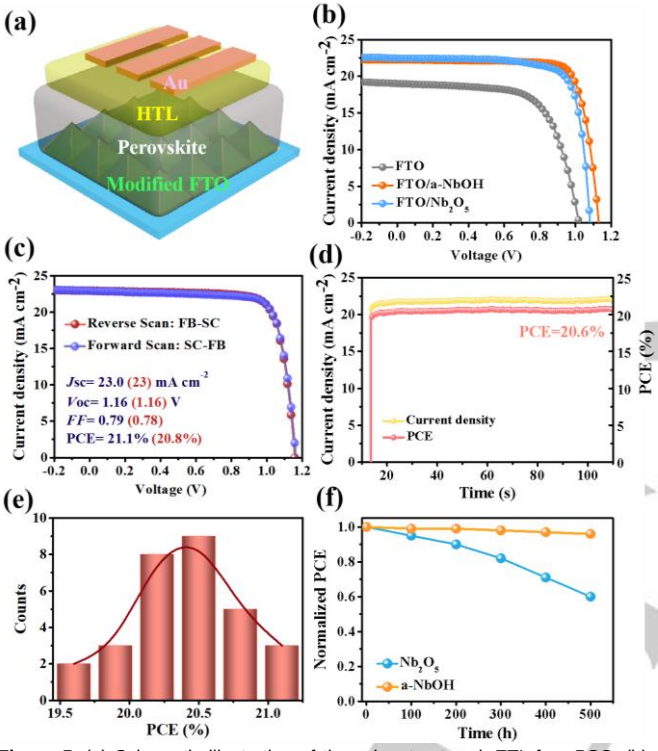

Figure 5. (a) Schematic illustration of the *n-i-p* structured, ETL-free PSC. (b) *J-V* characteristics of PSCs based on $MAPbI_3$ films deposited on different substrates. (c) *J-V* characteristics of PSCs fabricated using the $Cs_{0.07}FA_{0.70}MA_{0.23}PbI_3$ perovskite film deposited on a FTO/a-NbOH substrate measured at forward and reverse scan. (d) Steady-state photocurrent and stabilized PCE of the best-performing PSCs fabricated using the $Cs_{0.07}FA_{0.70}MA_{0.23}PbI_3$ perovskite film deposited on an FTO/a-NbOH substrate. (e) PCE histogram of a batch of 30 devices for the best-performing PSCs. (f) Operational stability of the encapsulated PSCs fabricated with FTO/a-NbOH and FTO/Nb_2O_5 substrates under constant one sun illumination.

Conclusion

We demonstrated that a non-annealed, ultrathin, amorphous metal oxide could alter the surface properties of TCO substrates for constructing efficient and stable ETL-free PSCs in a cost-effective, large-scale manner. The a-MOH showed moderate charge extraction rate but enabled largely suppressed charge recombination in PSCs. Considering that in PSCs the carrier recombination process is much slower than the carrier transfer process, we identified that the key factor in a high-performance ETL-free PSC was to suppress the charge recombination at the TCO/perovskite interface, as long as the electrons are collected by the TCO while the holes transfer pathway is blocked simultaneously. Simply coating an ultra-thin a-MOH layer on the TCO surface could play multifaceted roles, such as crystal growth modulation, interfacial defect passivation, electron tunneling and hole blocking. Encouragingly, the ETL-free PSCs delivered a champion PCE of 21.1% with negligible *J-V* hysteresis and improved operational stability. Additionally, this work displaces the necessity of employing a high temperature, annealed, metal oxide ETL, while providing a new insight to further improve the efficiency and stability of PSCs in the absence of charge transport layers.

Acknowledgements

The authors acknowledge the financial supports from Sun Yat-sen University, Discovery program and DECRA fellowship (DE180101190) of Australian Research Council (ARC).

Keywords: perovskite solar cells • interfacial modification • charge tunnelling • charge recombination • amorphous metal oxyhydroxide

[1] Q. Dong, Y. Fang, Y. Shao, P. Mulligan, J. Qiu, L. Cao, J. Huang, *Science* **2015**, *347*, 967-970.
[2] G. Xing, N. Mathews, S. Sun, S. S. Lim, Y. M. Lam, M. Grätzel, S. Mhaisalkar, T. C. Sum, *Science* **2013**, *342*, 344-347.
[3] W.-Q. Wu, Z. Yang, P. N. Rudd, Y. Shao, X. Dai, H. Wei, J. Zhao, Y. Fang, Q. Wang, Y. Liu, *Sci. Adv.* **2019**, *5*, eaav8925.
[4] J. Duan, Y. Zhao, B. He, Q. Tang, *Small*, **2018**, *14*, 1704443.
[5] Y. Rong, Z. Ku, A. Mei, T. Liu, M. Xu, S. Ko, X. Li, H. Han, *J. Phys. Chem. Lett.* **2014**, *5*, 2160-2164.
[6] H. Liu, Z. Chen, H. Wang, F. Ye, J. Ma, X. Zheng, P. Gui, L. Xiong, J. Wen, G. Fang, *J. Mater. Chem. A* **2019**, *7*, 10636-10643.
[7] B. Yang, M. Wang, X. Hu, T. Zhou, Z. Zang, *Nano Energy* **2019**, *57*, 718-727.
[8] Z. Li, Y. Zhao, X. Wang, Y. Sun, Z. Zhao, Y. Li, H. Zhou, Q. Chen, *Joule* **2018**, *2*, 1559-1572.
[9] Z. Song, C. L. McElvany, A. B. Phillip, L. Celik, P. W. Krantz, S. C. Watthage, G. K. Liyanage, D. Apul, M. J. Heben, *Energy Environ. Sci.* **2017**, *10*, 1297-1305.
[10] E. Halvani Anaraki, A. Kermanpur, M. T. Mayer, L. Steier, T. Ahmed, S.-H. Turren-Cruz, J. Seo, J. Luo, S. M. Zakeeruddin, W. R. Tress, T. Edvinsson, M. Grätzel, A. Hagfeldt, J.-P. Correa-Baena, *ACS Energy Lett.* **2018**, *3*, 773-778.
[11] Q. Liu, M. C. Qin, W. J. Ke, X. L. Zheng, Z. Chen, P. L. Qin, L. B. Xiong, H. W. Lei, J. W. Wan, J. Wen, G. Yang, J. J. Ma, Z. Y. Zhang, G. J. Fang, *Adv. Funct. Mater.* **2016**, *26*, 6069-6075.
[12] J. F. Liao, W. Q. Wu, Y. Jiang, J. X. Zhong, L. Wang, D. B. Kuang, *Chem. Soc. Rev.* **2020**, *49*, 354-381.
[13] Q. Han, J. Ding, Y. Bai, T. Li, J.-Y. Ma, Y.-X. Chen, Y. Zhou, J. Liu, Q.-Q. Ge, J. Chen, *Chem* **2018**, *4*, 2405-2417.
[14] P. Cui, D. Wei, J. Ji, D. Song, Y. Li, X. Liu, J. Huang, T. Wang, J. You and M. Li, *Solar RRL* **2017**, *1*, 1600027.
[15] Z. Hu, H. Xiang, M. S. Sebag, L. Billot, L. Aigouy, Z. Chen, *Chem. Commun.* **2018**, *54*, 2623-2626.
[16] J. F. Liao, W. Q. Wu, Y. Jiang, D. B. Kuang, L. Wang, *Solar RRL* **2019**, ***3***, 1800268.
[17] H. Yu, J. W. Lee, J. Yun, K. Lee, J. Ryu, J. Lee, D. Hwang, S. K. Kim and J. Jang, *Adv.Energy Mater.* **2017**, *7*, 1700749.
[18] L. Huang, D. Zhang, S. Bu, R. Peng, Q. Wei, Z. Ge, *Adv. Sci.* **2020**, *7*, 1902656.

[19] National Renewable Energy Laboratory (NREL),https://www.nrel.gov/pv/assets/pdfs/best-research-cell-efficiencies.20200406.pdf
[20] P. Zhao, M. Han, W. Yin, X. Zhao, S. G. Kim, Y. Yan, M. Kim, Y. J. Song, N. G. Park, H. S. Jung, *ACS Appl. Mater. Interfaces* **2018**, *10*, 10132-10140.
[21] D. Liu, J. Yang, T. L. Kelly, *J. Am. Chem.Soc.* **2014**, *136*, 17116-17122.
[22] W. Ke, G. Fang, J. Wan, H. Tao, Q. Liu, L. Xiong, P. Qin, J. Wang, H. Lei, G. Yang, *Nat. Commun.* **2015**, *6*, 1-7.
[23] Q. Wei, Z. Yang, D. Yang, W. Zi, X. Ren, Y. Liu, X. Liu, J. Feng, S. F. Liu, *Solar Energy* **2016**, *135*, 654-661.
[24] C. Huang, P. Lin, N. Fu, C. Liu, B. Xu, K. Sun, D. Wang, X. Zeng, S. Ke, *Chem.Commun.* **2019**, *55*, 2777-2780.
[25] Q. Hu, J. Wu, C. Jiang, T. Liu, X. Que, R. Zhu, Q. Gong, *ACS Nano* **2014**, *8*, 10161-10167.
[26] J. Pascual, I. Kosta, E. Palacios-Lidon, A. Chuvilin, G. Grancini, M. K. Nazeeruddin, H. J. Grande, J. L. Delgado and R. n. Tena-Zaera, *J. Phys. Chem. C* 2018, **122**, 2512-2520.
[27] D. Ouyang, Z. Huang, W. C. Choy, *Adv. Funct. Mater.* **2019**, *29*, 1804660.
[28] C. Liu, J. Yuan, R. Masse, X. Jia, W. Bi, Z. Neale, T. Shen, M. Xu, M. Tian, J. Zheng, *Adv. Mater.* **2020**, 1905245.
[29] W. Q. Wu, D. Chen, Y. B. Cheng, R. A. Caruso, *ACS Appl. Mater. Interfaces*, **2020**, *12*, 11450-11458.
[30] Z.-K. Zhou, Z.-H. Mo, X.-L. Wei, *Chem. Commun.* **2019**, *55*, 11916-11919.
[31] D. C. Wu-Qiang Wu, Yi-Bing Cheng, Rachel A. Caruso, *Solar RRL* **2017**, ***1***, 1700117.
[32] Z. Zhu, Y. Bai, T. Zhang, Z. Liu, X. Long, Z. Wei, Z. Wang, L. Zhang, J. Wang, F. Yan, *Angew. Chem. Int. Ed.* **2014**, *126*, 12779-12783.
[33] T. Wu, Y. Wang, X. Li, Y. Wu, X. Meng, D. Cui, X. Yang, L. Han, *Adv. Energy Mater.* **2019**, *9*, 1803766.
[34] W. G. Li, X. D. Wang, J. F. Liao, Y. Jiang, D. B. Kuang, *Adv. Funct. Mater.* **2020**, *30*, 1909701.
[35] X. Liu, Y. Cheng, C. Liu, T. Zhang, N. Zhang, S. Zhang, J. Chen, Q. Xu, J. Ouyang, H. Gong, *Energy Environ. Sci.* **2019**, *12*, 1622-1633.
[36] Z. Zhu, J. Ma, Z. Wang, C. Mu, Z. Fan, L. Du, Y. Bai, L. Fan, H. Yan, D. L. Phillips, *J. Am. Chem.Soc.* **2014**, *136*, 3760-3763.
[37] Q. Wang, Q. Dong, T. Li, A. Gruverman, J. Huang, *Adv. Mater.* **2016**, *28*, 6734-6739.
[38] K. Wu, G. Liang, Q. Shang, Y. Ren, D. Kong, T. Lian, *J. Am. Chem. Soc.* **2015**, *137*, 12792−12795.
[39] F. Zhang, C. Yi, P. Wei, X. Bi, J. Luo, G. Jacopin, S. Wang, X. Li, Y. Xiao, S. M. Zakeeruddin, *Adv. Energy Mater.* **2016**, *6*, 1600401.
[40] W. Q. Wu, P. N. Rudd, Z. Yang, J. Huang, *Adv. Mater.* **2020**, *32*, 2000995.
[41] W.Q. Wu, P. N. Rudd, Z. Ni, C. H. Van Brackle, H. Wei, Q. Wang, B. R. Ecker, Y. Gao, J. Huang, *J. Am. Chem. Soc.* **2020**, *142*, 3989-3996.

Entry for the Table of Contents

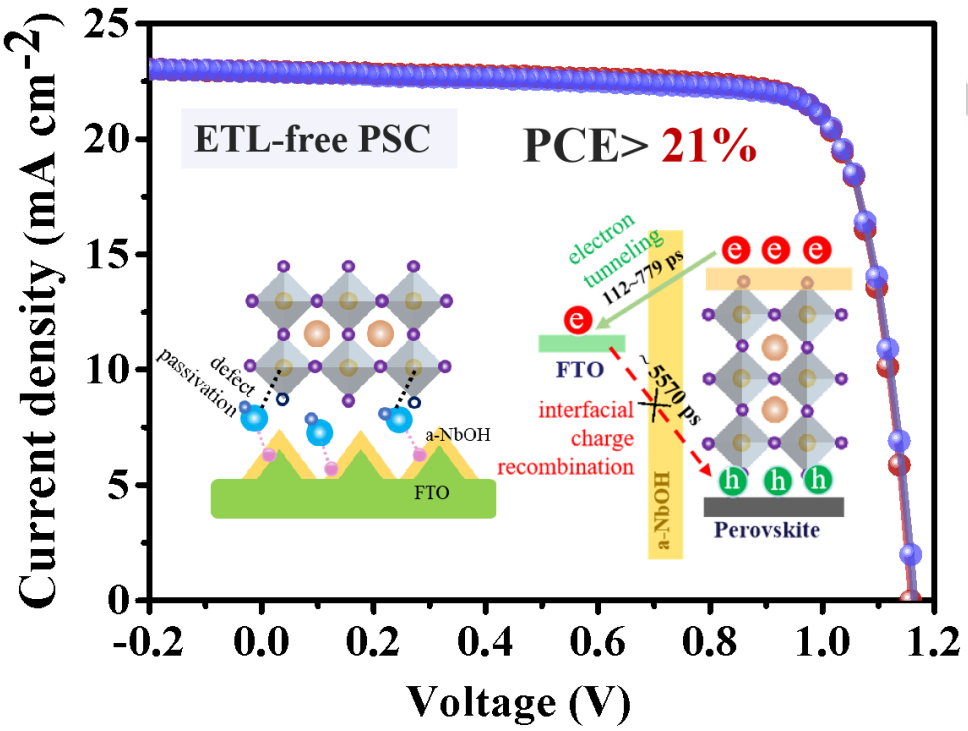

A non-annealed, ultrathin, amorphous metal oxyhydroxide was introduced to suppress interfacial charge recombination and reduce energy loss in ETL-free perovskite solar cells, achieving a record efficiency of 21.1%.